MECHANICS OF ELECTRODES IN HIGH CAPACITY LITHIUM-ION BATTERIES

A Thesis

by

GARRETT RANSFORD HARDIN

Submitted to the Office of Graduate and Professional Studies of
Texas A&M University
in partial fulfillment of the requirements for the degree of

MASTER OF SCIENCE

Chair of Committee,	Matt Pharr
Committee Members,	Chandler Benjamin
	Harry Hogan
Head of Department,	Daniel McAdams

August 2018

Major Subject: Mechanical Engineering

ABSTRACT*

Lithium ion batteries (LIBs) have become the power source of choice for portable electronics and electric vehicles. With growing demand in these applications, batteries now require higher capacities, energy densities, and longer cycle lives. To meet these demands many new high capacity materials and electrode architectures are being researched but mechanical degradation during cycling has precluded their use in practical applications. At the same time, little is known regarding the mechanical properties of these high capacity electrodes during cycling.

In this work, we begin by investigating interfacial detachment of nanowires (NW) from current collectors (CC) due to volume changes during cycling by performing finite element analyses to calculate the energy release rate under various conditions. The simulations show that the energy release rate of a surface crack decreases as it propagates along the NW/CC interface toward the center of the NW. Moreover, this work demonstrates that plastic deformation in the NWs drastically reduces stresses and thus the crack-driving forces, thereby mitigating interfacial fracture.

This work also investigates the stress response and change in material properties of a V_2O_5 thin film cathode during lithiation. We utilize nanoindentation to measure the hardness and elastic modulus of $Li_xV_2O_5$ as a function of lithium concentration. We also use a multi-beam optical sensor (MOS) to measure substrate curvature and Stoney's equation to calculate stresses in the film.

We found that as lithium concentration increases, the modulus of $Li_xV_2O_5$ also sees a general increase, while the hardness sees an initial increase though the δ phase followed by a decrease in both the γ and ω phases. The stress of the electrode correlates well with the "a" lattice parameter, which is aligned parallel to the surface of the substrate. The stress also demonstrates interesting sudden inflection points at times when multiple phases coexist. Once the electrode is cycled into the ω phase it becomes a rock-salt structure and exhibits an amorphous like stress accumulation.

Overall, the results in this work provide instrumental data and guidelines for designing electrodes in high capacity batteries that will avoid mechanical degradation during electrochemical cycling.

DEDICATION

I would like to dedicate this work to my father, who has always been my primary role model in my life. I have followed many of his steps in life (while trying to best his results along the way), and he has always provided a path and the gentle guidance which has lead me to the position I am in today. As Isaac Newton once said “If I have seen further it is by standing on the shoulders of giants,” and he will always be my personal giant.

ACKNOWLEDGEMENTS

I would like to thank my committee chair, Dr. Matt Pharr, for his countless hours of guidance, support, and his timeless advice to “fail quickly”. I would also like to thank my friends and colleagues in the Experimental Solid Mechanics Laboratory for their help and companionship throughout the course of this research. Finally, I would like to thank my parents for enabling me to continue in my educational journey and always lovingly and enthusiastically supporting me in all my endeavors.

CONTRIBUTORS AND FUNDING SOURCES

A thesis committee consisting of Professor Matt Pharr and Professors Harry Hogan and Chandler Benjamin of the Department of Mechanical Engineering, and Professor Terry Creasy of the Department of Material Science & Engineering supported this work.

The analysis provided in Chapter II was conducted in part by Cole Fincher and Yuwei Zhang of the Department of Mechanical Engineering at Texas A&M University and was published in 2017 in an article listed in JOM Volume 69, Issue 9, pp 1519-1523. The analysis provided in Chapter III was conducted in part by Cole Fincher and Yuwei Zhang of the Department of Mechanical Engineering at Texas A&M University and David Santos of the Department of Chemistry at Texas A&M University.

Graduate study was supported by Matt Pharr's startup funds from Texas A&M University, the Department of Mechanical Engineering at Texas A&M University, the Texas A&M University Engineering Experiment Station, as well as the Teaching Assistant program for the Department of Mechanical Engineering at Texas A&M University.

NOMENCLATURE

LIB	Lithium Ion Battery
NW	Nanowire
CC	Current Collector
ITO	Indium Tin Oxide
XRD	X-Ray Diffraction
MOS	Multi-beam Optical Sensor

TABLE OF CONTENTS

Page

LIST OF FIGURES

Page

LIST OF TABLES

Page

CHAPTER I

INTRODUCTION AND LITERATURE REVIEW

*Introduction**

Lithium ion batteries (LIBs) have become an ever increasing part of our everyday life. They are the power source of choice for innovative technologies such as portable electronics and electric vehicles and provide a means of storing power from alternative sources of renewable energy[1-2]. With growing demand, these applications now require batteries with higher capacities, energy densities, and longer cycle lives [3-5]. To meet these demands many new materials and electrode architectures are being researched, but little is known about the mechanical properties and behaviors of these new high capacity electrodes. Studying these mechanical properties will allow for modeling and prediction of how future battery cells will behave and aid in the design of future high capacity LIBs that avoid mechanical degradation.

*Si Nanowires**

Many electrodes are often nano-structured in the form of thin films, nanopillars, nanoparticles, or nanowires (NWs) [6-8]. NWs are particularly popular due to the open space between them into which individual NWs can freely swell, thereby reducing stresses in the electrodes [9-10]. These configurations also introduce shorter diffusion distances for the Li-ions, thus enabling high charge/discharge rates [7, 11-12]. However, despite their advantages, NWs can still suffer mechanical degradation. For instance, Nguyen et al. found Si NWs floating in the electrolyte after cycles of lithiation/de-lithiation due to detachment of the NWs from the CC [10].

In addition to Si, NW electrodes of Ge, Co_3O_4, TiO_2, and SnO_2 have been implemented in LIBs [13-17].

Despite the prevalence of NWs in LIBs, only a few studies have analyzed the mechanics of their fracture. Ryu et al. studied lithiation of Si NWs and found a critical radius of 300 nm, below which internal fracture was averted in both simulation and experiment [18]. Liu et al. [19] also studied lithiated Si NWs and found anisotropic swelling under certain conditions, which resulted in large tensile hoop stresses which propagated internal cracks. While internal fractures of NWs have been studied, no mechanical studies have addressed a separate key concern: lithiation-induced detachment of the NW from the CC. During lithiation, the NW expands but the CC does not. As a result, stresses are generated near the root of the NW, which may lead to detachment from the CC, thus diminishing the capacity of the battery [10].

Vanadium Oxide

Vanadium oxides demonstrates many interesting optical and chemical properties and have thus been exploited in applications such as smart windows[20-22], sensors[23-24], and lithium-ion batteries[25-28]. For applications in batteries, two compounds of vanadium oxide stand out as potential cathode materials, V_2O_5 and VO_2(B) [29-31]. Both of these compounds provide relatively high theoretical capacities to host lithium as compared to traditional cathode materials and have demonstrated excellent cyclability. In particular, V_2O_5 has demonstrated low capacity loss even at extremely large charging/discharging rates when cycled within certain phases [31-32]. This thesis will focus on V_2O_5 and leave VO_2(B) as future work.

Despite extensive research on V_2O_5, little is known regarding the mechanics of lithiated vanadium oxide, $Li_xV_2O_5$. Scarminio et al. and Talledo et al. used beam deflectometry to explore

these properties in the 1990's and studied how mechanical stresses develop in thin films of V_2O_5 during lithiation [33-34]. These studies provided qualitative data of stress evolution in these films and demonstrated a strong correlation between changes in lattice parameters and stress development. More recently, Jung et al. used optical interferometry to measure stress development over a larger range of lithiation and different charging rates [35-36]. However, these studies make assumptions of constant mechanical and volumetric properties and only provide quantitative data over a small range of lithiation. This work will provide a quantitative analysis of the stress development in $Li_xV_2O_5$ films over the entire lithiation range, as well as characterize hardness and elastic modulus of $Li_xV_2O_5$ with the goal of providing invaluable data for future modeling applications. The hardness and elastic modulus for lithiated V_2O_5 have never been measured before, despite most modeling and stress calculations requiring them.

CHAPTER II

SI NANOWIRES*

This chapter analyzes detachment of NW electrodes from CCs during electrochemical cycling. We implemented finite element simulations to calculate the energy release rate associated with the propagation of a surface flaw during lithiation. The simulations also reveal the dependence of the energy release rate on the crack length, aspect ratio, NW radius, and yield strength. Overall, the results in this chapter provide design guidelines for averting NW/CC interfacial fractures during operation of LIBs.

Numerical Procedure

To simulate interfacial fractures along the NW/ CC interface, we performed finite element simulations in ABAQUS. The NW electrode is represented by an axisymmetric model of length h, radius r, and surface-crack length a as shown in Figure 1. Here, we implement an axisymmetric model for simplicity due to the absence of experimental data regarding the precise shape of the flaws at the NW/CC interface.

Additionally, the crack driving force depends primarily on the length of the crack and less so on the precise shape (e.g., the width of the crack). During the initial step, the base of the NW was fixed to represent the constraint that the CC places on it. With this constraint in place, the NW swells due to the insertion of the lithium.

*This chapter has been reprinted with permission from "Interfacial Fracture of Nanowire Electrodes of Lithium-Ion Batteries" by G. R. Hardin, Y. Zhang, C. D. Fincher et al, 2017. JOM Journal of the Minerals, Metals and Materials Society, 69, 9, Copyright 2017 by Springer Nature.

We simulate this step by implementing thermal swelling to the same level of volume expansion associated with lithiation of the material (Figure 1b). As an example, Si swells by 280% upon lithiation to the fully lithiated state of $Li_{3.75}Si$ [37-38]; a corresponding level of thermal strain was implemented to simulate these conditions, with large deformation taken into account (Nlgeom enabled in ABAQUS). In this step, it is assumed that enough time is allowed for diffusive equilibrium (e.g., as during slow charging) such that the concentration of lithium is uniform in the NW. We make this assumption due to the mechanics of the constraint of the CC near the NW/ CC interface; large stresses develop near this interface regardless of the precise lithiation kinetics. Likewise, we do not consider the effects of a two phase reaction-controlled process, as have been observed in some studies [39-42].

In the final step, a crack of length a is introduced by opening a free surface of length a, starting at the surface of the NW and propagating along the NW/CC interface, as shown in Figure 1c. The length of the crack is incrementally increased toward the center of the NW. During each step, ABAQUS computes the stresses and strains in the NW. The constitutive model employed in ABAQUS is essentially elastic-perfect-plastic but with a small amount of artificial strain hardening added to mitigate numerical issues in the simulation, i.e., to ensure convergence.

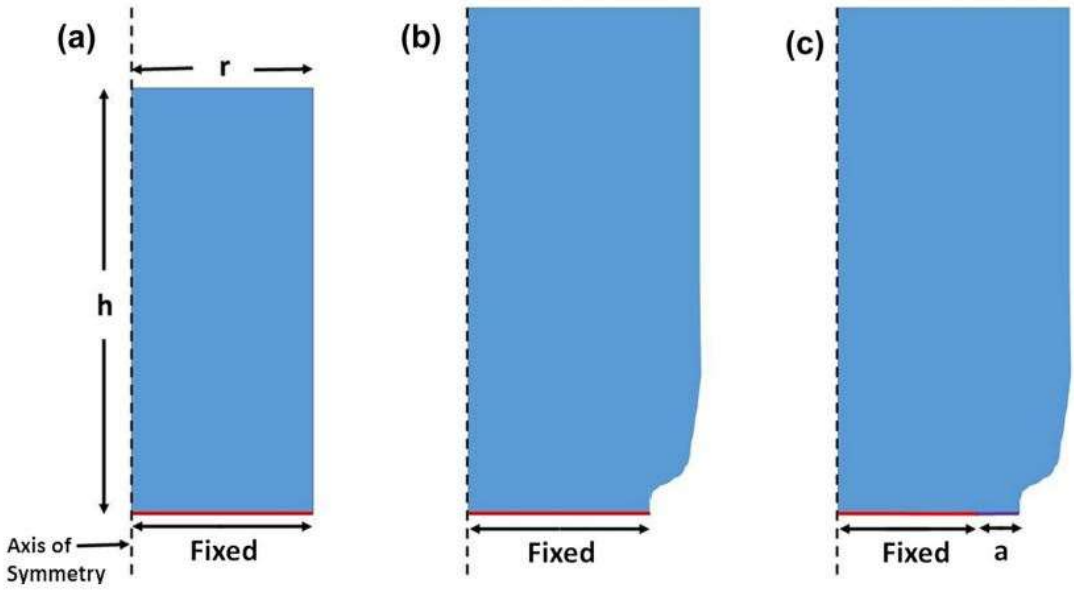

Figure 1. Schematics of a nanowire during the ABAQUS simulations. (a) The nanowire prior to lithiation and corresponding dimensions. (b) The nanowire as it expands during lithiation. The nanowire is fixed along the interface with the current collector, and the strain energy, U_1, is computed. (c) A free surface of length a is introduced to represent a crack. The strain energy, U_2, is calculated. The difference between the strain energies in (b) and (c) determines the crack driving force through Eq. 1. Reproduced with permission from [43].

To calculate the crack driving force, we follow a method developed by Choi et al. [44] in the context of thin film silicon anodes. They successfully calculated the energy release rate in ABAQUS by computing the incremental change in the internal energy as the crack advances by a unit area. The energy release rate, G, is calculated as follows:

$$G = -\frac{\partial U}{\partial A} = -\frac{U_i - U_{i-1}}{A_i - A_{i-1}}, \quad (1)$$

where U_i represents the internal energies in the system when a crack is of a certain length (at step *i*) and A_i the areas of the uncracked regions at the same step, i.e., the quantity $(A_i - A_{i-1})$ represents the area swept out by the crack during step *i*. In ABAQUS, the internal energy includes

both the recoverable strain energy as well as the energy dissipated by plastic deformation. Following standard practice [45], the crack driving force can also be written in the form:

$$G = Z\overline{E}\varepsilon^2 a, \tag{2}$$

where Z is a pre-factor that is a function of nondimensional variables, $\overline{E} = E/(1-\nu^2)$ is the plane strain modulus, ν the Poisson's ratio, ε the strain (in this case from thermal strain), and α the length of the crack. In this study, we will primarily examine the effects of non-dimensional parameters contained in the pre-factor, $Z = f(\frac{\sigma_Y}{E}, \frac{a}{R}, \frac{h}{R})$, on the energy release rate. The three non-dimensional parameters represent the effect of plasticity, crack size (or NW radius), and aspect ratio, respectively, on the energy release rate.

Results and Discussion

Figure 2 shows the energy release rate as a function of crack size after full lithiation of a Si NW, which corresponds to 280% volume expansion. The NW had a radius of 200 nm, a height of 600 nm, and the material properties listed in Table I reported previously by Pharr et al [44]. The horizontal line in Figure 2 indicates an interfacial fracture energy of Γ_i= 1.5 J/m^2, which is representative of the interfacial energy of a $Li_{3.75}Si$/Cu interface [46]. The simulation models the evolution of the crack driving force as the crack advances incrementally toward the center of the NW. As can be seen in Figure 2, the energy release rate monotonically decreases to zero as the crack advances toward the center of the NW. This phenomenon occurs because, as the crack length approaches the radius of the NW, most of the stresses in the NW have already been relaxed, and thus the crack driving force has diminished. This result represents a key advantage of a NW electrode. That is, from our modeling, we predict that a NW will never completely delaminate from the CC due to lithiation alone. Specifically in our simulation of a fully lithiated silicon NW,

propagation of a crack is no longer energetically favorable once $G < \Gamma_i$, represented by the intersection of the black curve with the horizontal red dashed curve in Figure 2. At this point, the crack will arrest and the NW will not completely delaminate from the CC.

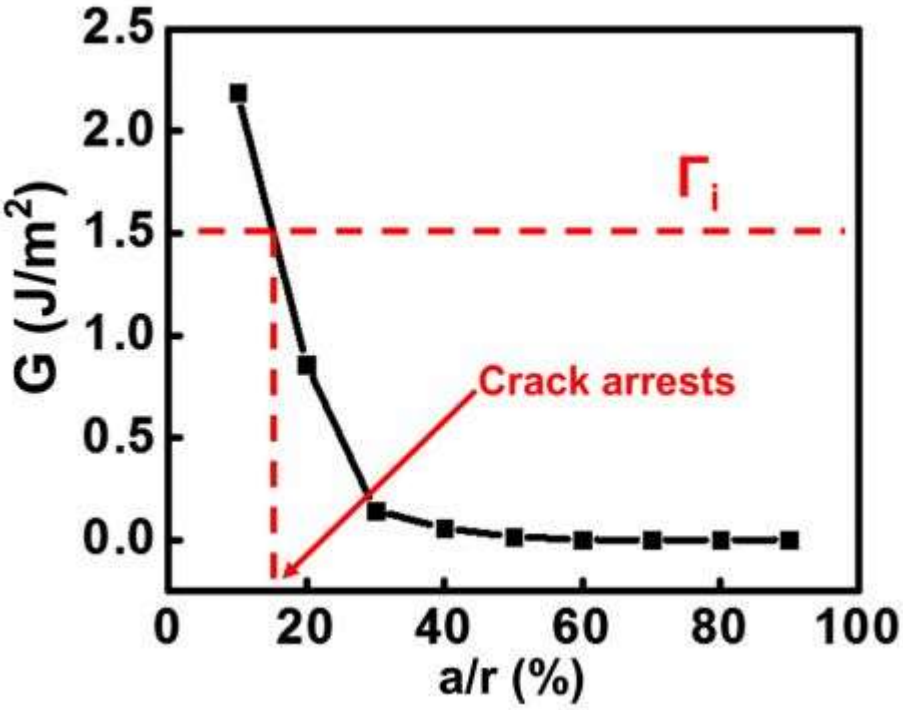

Figure 2. The energy release rate as a function of crack length (normalized by the radius of the NW) after full lithiation of a Si NW. The horizontal red dashed line indicates a representative value of the interfacial fracture energy of a $Li_{3.75}Si$/Cu interface. Reproduced with permission from [43].

Table 1. Mechanical properties of lithiated silicon [44]

	Li_0Si	$Li_{0.47}Si$	$Li_{1.47}Si$	$Li_{2.34}Si$	$Li_{3.28}Si$	$Li_{3.75}Si$
Young's modulus E (GPa)	113	59	50	43	32	32
Yield strength σ_Y (MPa)	166	800	540	460	340	340
Poisson's ratio (v)	0.25					

Even if our simulations predict that a NW never entirely delaminates from the CC, crack propagation still has detrimental effects on the system. Crack propagation decreases the contact area between the NW and the CC. As a result, the area of the conducting path for electrons from

the CC to the NW decreases, thereby increasing the resistance of the electrode. Similarly, if the crack propagates a large distance, only a small ligament remains that connects the NW to the CC. The remaining NW will be much more susceptible to full debonding due to subsequently applied external loads.

As an additional note regarding Figure 2, we also simulated Si NWs lithiated to various states of charge. We found that the maximum energy release rate occurs upon full lithiation, so this work focuses on this critical worst-case scenario. We also simulated de-lithiation of a Si NW and found that the maximum energy release rates were much smaller than during lithiation. As a result, here, we focus on lithiation. We also performed simulations to evaluate the influence of the mechanical properties of the NW on interfacial fracture. To do so, we varied the yield strength in the simulations relative to the elastic modulus; the results are shown for a NW with a 200-nm radius and a 600-nm height for 10% volume expansion in Figure 3. For reference, from Table 1, $Li_{0.47}Si$ has a value of $\sigma_Y/E = 1.4\%$. Figure 3 clearly indicates that the crack driving force increases monotonically with the yield strength of the material. This phenomenon occurs because the NWs are subjected to large swelling strains during lithiation. However, the yield strength of the NW sets a bound on the stress that can build up in the system. Smaller stresses due to smaller yield strengths result in smaller crack driving forces, as there is less stress to relax in the system.

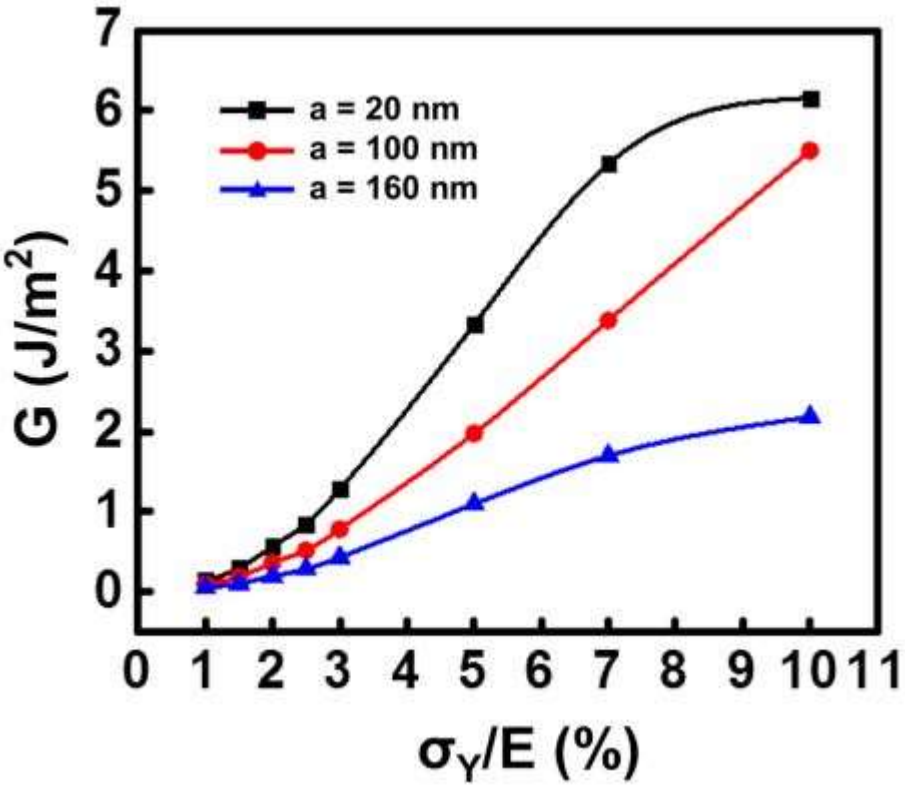

Figure 3. The energy release rate as a function of the yield strength (normalized by the elastic modulus) for h/r = 3 and volumetric expansion of 10%. Reproduced with permission from [43].

Figure 4 demonstrates the influence of the aspect ratio of the NW, h/r, on the energy release rate for a fully lithiated Si NW. The plot shows the energy release rate for a specific value of a/ r = 10% ($G_{a/r=10\%}$) as a function of crack length. In the simulation, we used the material properties in Table 1. The key feature of this plot is that the energy release rate plateaus to a constant value above an aspect ratio of around h/r = 1. In other words, the energy release rate of a NW (for which $h/r \gg 1$) does not depend on the aspect ratio of the NW. Thus, all the simulations performed in this work apply equally well to NWs of any aspect ratio. The phenomenon can be explained by considering the mechanics of the constraint placed on the NW by the CC. Stresses exist near the NW/CC interface in a region whose height scales with the radius of the NW. At

distances (in the vertical direction) larger than this, the NW is stress-free. Thus, making the NW taller only adds unstressed regions to the NW and thus does not contribute to the energy release rate. As a final note related to Figure 4, we should comment that in the previous analyses (e.g., Fig. Figure 2 & Figure 3), we have used a relatively small aspect ratio of h/r = 3. However, Figure 4 demonstrates that even this small aspect ratio is already in the plateau region. Thus, the previous simulations (Fig. Figure 2 & Figure 3) are indeed representative of the physics of a NW.

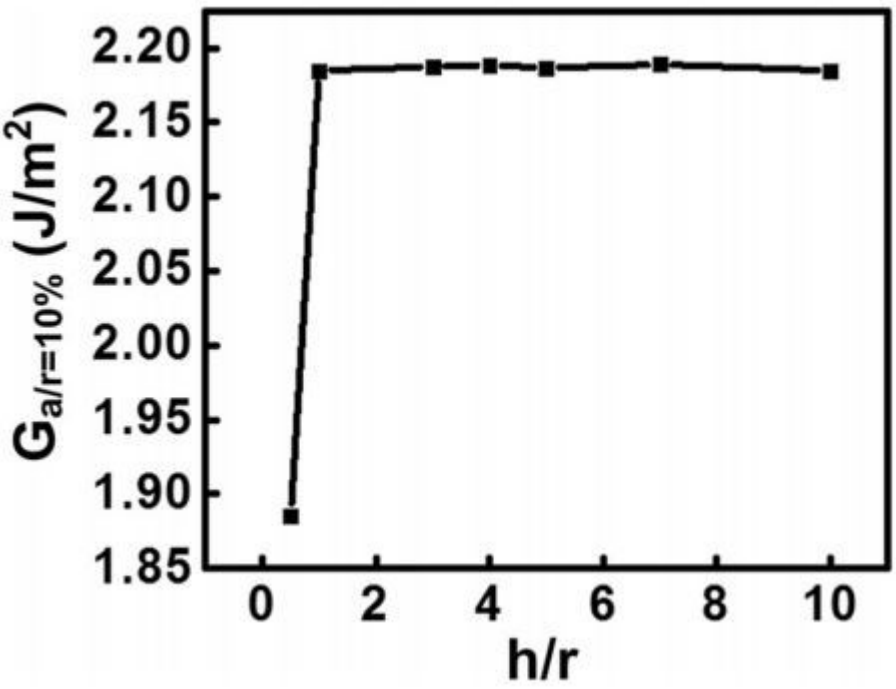

Figure 4. The maximum energy release rate as a function of the aspect ratio of fully lithiated Si NW. Reproduced with permission from [43].

Although the aspect ratio does not influence the energy release rate, the radius itself does. Figure 5 shows the dependence of the crack driving force (at a particular value of a/r = 10%) on the radius of the NW. We use the material properties listed in Table 1 and a fixed aspect ratio of h/r = 3 in the simulations. The plot shows that the energy release rate scales linearly with the radius of the NW. This result is intuitive in that the volume over which energy is dissipated when a crack

advances across the entire CC/NW interface should scale as r^3 , while the area of the crack scales as r^2 , thus leading to a linear scaling of the crack driving force with the radius of the NW (for a fixed value of h/r). As mentioned previously, crack propagation has detrimental effects on the electrode and thus should be avoided.

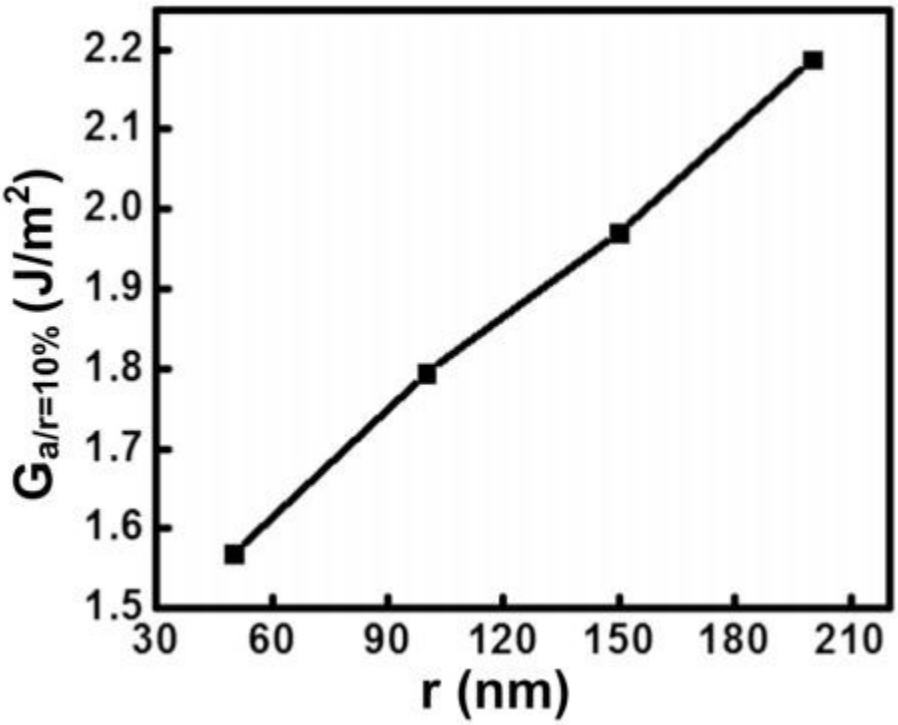

Figure 5. The maximum energy release rate as a function of the radius of a fully-lithiated Si NW with an aspect ratio of $h/r = 3$. Reproduced with permission from [43].

CHAPTER III

VANADIUM OXIDE

This chapter analyzes the stress development during lithiation of vanadium oxide (V_2O_5) cathodes. It also characterizes the elastic modulus and hardness of $Li_xV_2O_5$ as a function of lithium concentration.

Experimental Procedure

Vanadium oxides were deposited using RF reactive ion sputtering. The target was a 2" diameter vanadium metal (99.7% purity) target. The substrates used were a 12.7 mm diameter mirror polished stainless steel disk for MOS measurements and a 12 mm x 12 mm indium tin oxide (ITO) coated float glass slide (Delta Technologies CB-50IN-0105) for nanoindentation measurements. The substrates were initially cleaned by a rinse of acetone, isopropanol, and then deionized water, which was repeated twice. The substrate was then placed in the sputtering chamber and the deposition conditions were as follows: $< 10^{-8}$ Torr base pressure, 7.5 mTorr working pressure, 200 W RF power, and 36 cm working distance. The substrate was heated to 400^{o}C and oxygen and argon were flowed at 3.6 sccm and 20 sccm, respectively. Pre-sputtering took place with only argon flowing for 5 minutes followed by another 5 minutes with oxygen also flowing. After deposition the heat source was removed and the substrate was allowed to cool naturally in a vacuum environment. A film of 140 nm and 530 nm was deposited on stainless steel and ITO coated glass, respectively. The film thickness was measure by a Bruker DektakXT Surface Profiler.

Phase assignment was performed by X-ray Diffraction (XRD) using a Bruker D8 Advance Bragg−Brentano X-ray powder diffractometer with Cu Kα radiation (λ = 1.5418 Å). Figure 6

shows the diffraction pattern of a V_2O_5 thin-film prepared on an ITO coated glass substrate. Here, peak positions in 2θ at 20.26° and 41.26° correspond to the (001) and (002) lattice planes, respectively, thereby demonstrating preferential growth of orthorhombic α-V_2O_5 (JCPDS #41-1426) with *Pmmn* space group symmetry, with the c-axis perpendicular to the plane of the substrate. This preferential growth is in good agreement with previous reports [47-49]. The remaining reflections can be assigned to the underlying ITO substrate. No additional reflections evident of impurities are present in the x-ray diffraction data, thereby indicating that the films consist of a pure phase of α-V_2O_5.

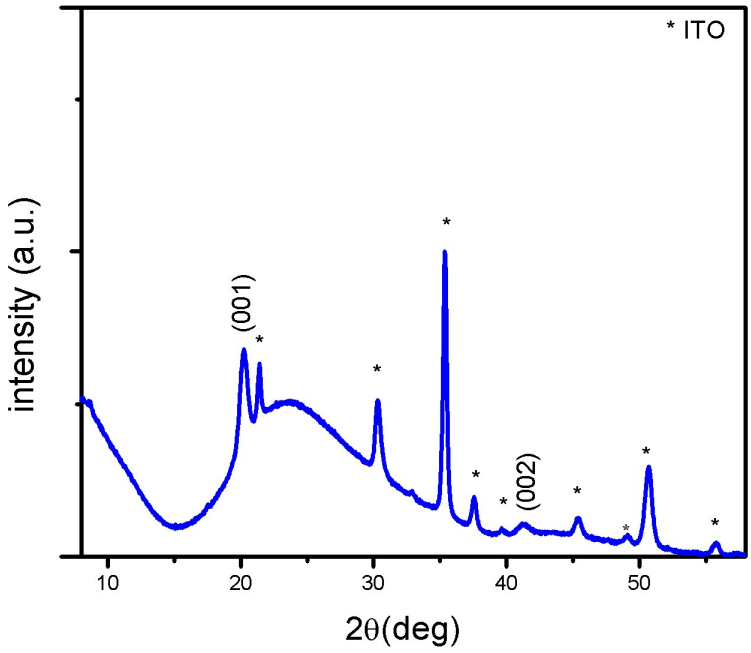

Figure 6. Powder XRD pattern of V_2O_5 thin-film (λ= 1.5418 Å). The reflections corresponding to V_2O_5 are labeled as (hkl) and the symbol * is used to denote the reflections of the underlying ITO substrate.

In addition, Raman spectra was collected by a Jobin-Yvon HORIBA LabRAM HR800 instrument coupled to an Olympus BX41 microscope. Spectra were collected with excitation from

the 514.5 nm line of an Ar-ion laser. Figure 7 displays the Raman spectra of a V_2O_5 thin film prepared on ITO coated glass. The frequencies of the nine Raman bands between 100-1000 cm^{-1} can be assigned to the α-V_2O_5 polymorph and are in good agreement with the existing literature [50-51]. Moreover, the peaks are well-resolved, thereby indicating good crystallinity. Once again, a pure and single phase is evident here, as no other peaks were observed.

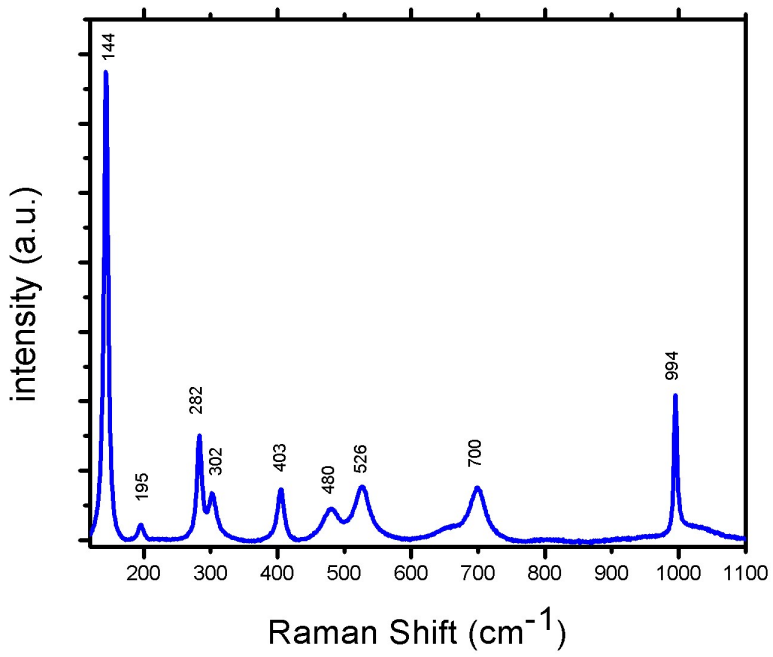

Figure 7. Raman spectrum of V_2O_5 thin-film using an excitation of 514.5 nm.

Electrochemical cycling of the electrodes was conducted in a split-cell with a 1.92 mm thick quartz window (MTI EQ-STC-QW) for MOS measurements and a quick assembly coin cell (MTI EQ-HSTC) for samples undergoing indentation. The cells were assembled in an argon-filled glovebox in a two-electrode configuration with Li as the counter electrode and a solution of 1 mol/L $LiPF_6$ in EC+EMC solvent with a 3:7 volumetric ratio (MTI EQ-LBC3015B-LD) as an electrolyte. After assembly the batteries were cycled using a PARSTAT MC Multichannel

Potentiostat at a rate of 1/12 C and 1/5 C for MOS and indentation tests respectively using a theoretical capacity of 441 mAh/g, a density of 3.36 g/cm^3, and measured thickness and area [31].

Nanoindentation

Assuming the vanadium oxide film is homogeneous and has a rate-independent elastic modulus on the same order of magnitude as the sputtering substrate, then the indentation sample can be modelled using the thin film model of Hay and Crawford [52]. As illustrated in Figure 8, the shear moduli are modelled as a set of springs in series, weighted as according to the ratio of the contact radius to film depth. As both the film and substrate are indented, both the substrate and the film deform as springs in parallel, while a spring in series is added to model the lateral support of the film as the indentation depth increases. Using this model along with the Oliver-Pharr approach [53] to determine contact area, the displacement and stiffness measurements were used to estimate the modulus and hardness of the vanadium oxide films.

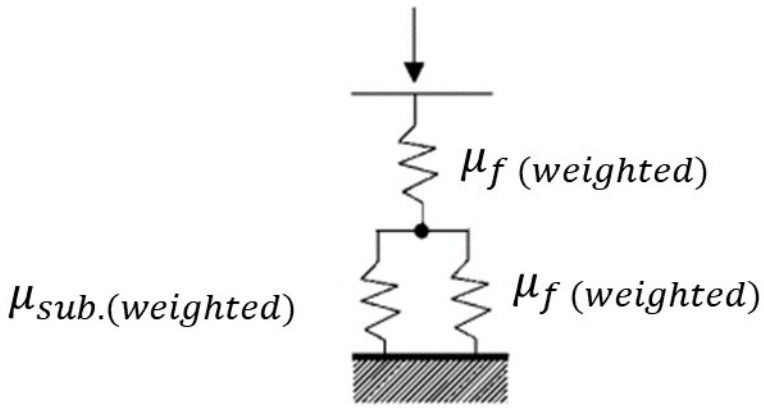

Figure 8. A schematic of the spring system used in the Hay and Crawford model [52], where the shear modulus are weighted as according to the ratio of contact diameter to film thickness.

The elastic modulus and hardness of the vanadium oxide cathode were measured using a Nanomechanics iMicro nanoindenter with an InForce 50 actuator. The displacement, stiffness, and hardness were recorded over nanoindentation tests conducted to a depth of 40% of the film thickness, using a loading rate of $0.2\ \frac{1}{s}$, and a continuous stiffness measurement amplitude and frequency of 1.75 nm and 100 Hz, respectively.

Multi-beam Optical Sensor

Substrate curvature measurements were taken with a k-Space Associates Multi-beam Optical Sensor (MOS). Figure 9 depicts the MOS set up where a laser is split in to parallel beams by a set of etalons. These beams then reflect off the back of the electrode and their positions are recorded by a CCD camera. The change in curvature is calculated from the geometric relation

$$\Delta K = \frac{(d_0 - d)}{d_0}\left[\frac{cos\alpha}{2L}\right] \quad (2)$$

where d is the distance between two adjacent laser spots captured on the CCD, d_0 is the initial distance between the laser spots, α is the angle of refraction of the laser beams, and L is the distance between the CCD camera and electrochemical cell [3].

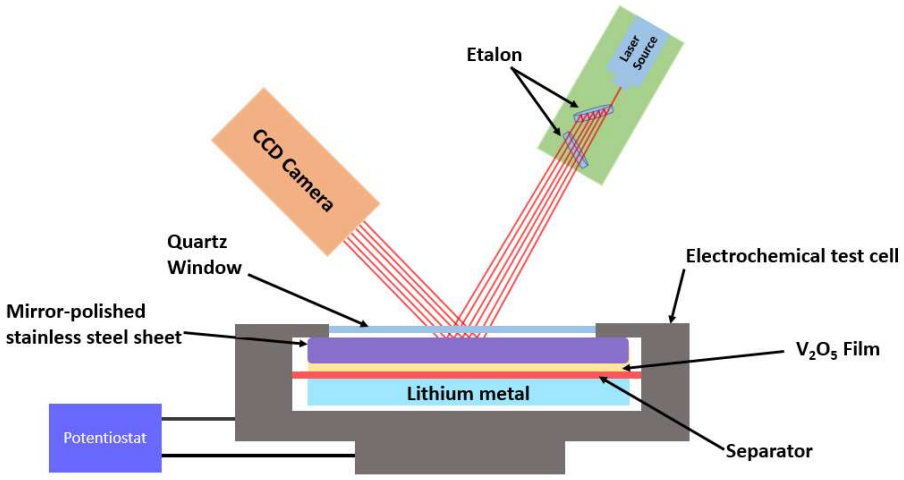

Figure 9. Depiction of Multi-Beam Optical Sensor (MOS) setup used to measure substrate curvature.

The average stress in the film during cycling was deduced by the measured change in curvature of the substrate and Stoney's Equation [54-55]:

$$\Delta\sigma = \frac{E_s h_s^2}{6h_f(1-\nu_s)}\Delta K, \quad (3)$$

where $\Delta\sigma$ is the average change in stress in the film, E_s is the elastic modulus of the substrate, h_s and h_f is the thickness of the substrate and film respectively, ν_s is the Poisson's ratio of the substrate, and ΔK is the change in curvature. In the equation, the values of E_s= 203 GPa, h_s = 0.736 mm, and ν_s = 0.29 were used for the substrate.

Due to the highly aligned crystalline nature of V_2O_5, the relative change in thickness of the film is expected to vary linearly with the change in the lattice parameter "c", which is perpendicular to the substrate. The values of this lattice parameter for $Li_xV_2O_5$ were reported by Jung et al. and used to calculate h_f in equation) [35] $\Delta\sigma = \frac{E_s h_s^2}{6h_f(1-\nu_s)}\Delta K$.

Results and Discussion

Figure 10 below shows a representative discharge curve of one of the V_2O_5 electrodes. As the electrode discharges it goes through a series of phase transformations; plateaus in the curve indicate regions in which two phases coexist. The $\alpha, \epsilon,$ and δ phases are all orthorhombic; cycling into these phases is reversible. The next phase, γ, is partially irreversible and also orthorhombic but has significant puckering or buckling of the V_2O_5 layers, as can be seen in Figure 11 [56]. As the V_2O_5 finally transforms to the ω phase it becomes a weakly crystalline rock-salt structure; cycling into this phase is irreversible [36].

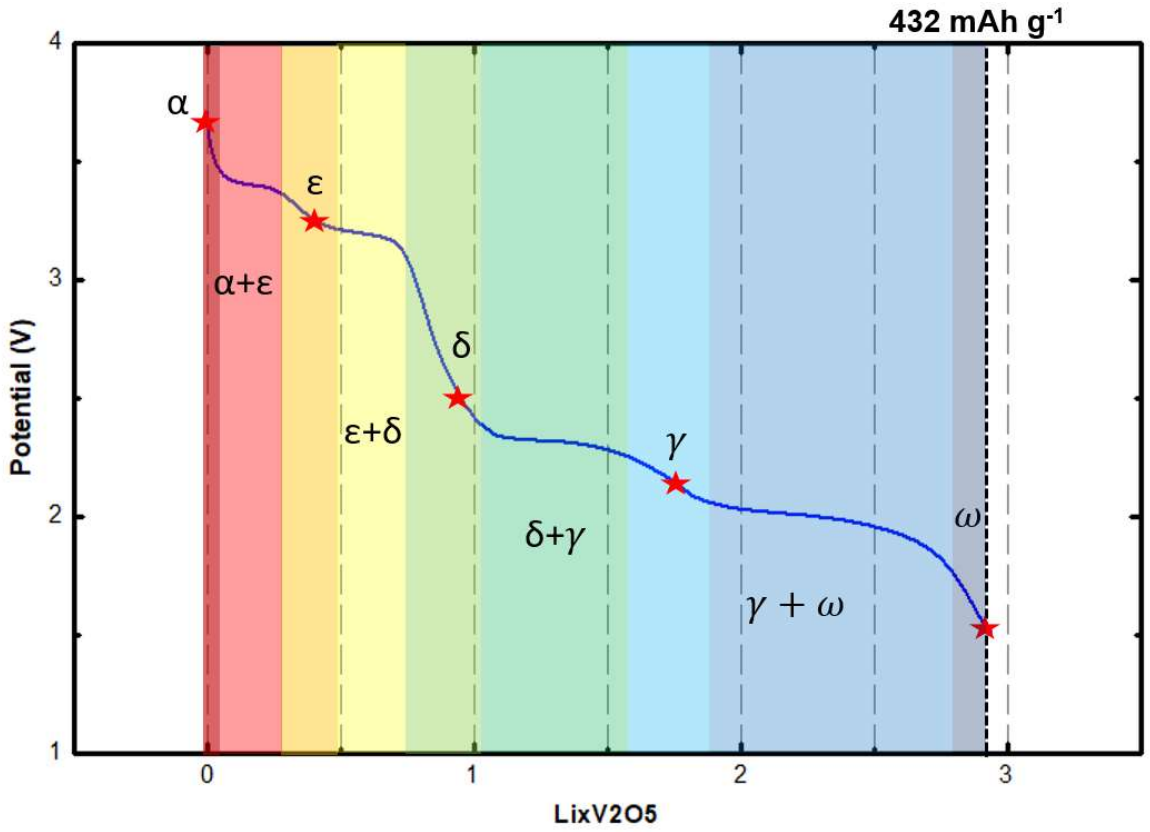

Figure 10. Example discharge curve showing the ranges of various V_2O_5 phases. The red stars indicate positions at which cells were disconnected while in a single phase for nano-indentation.

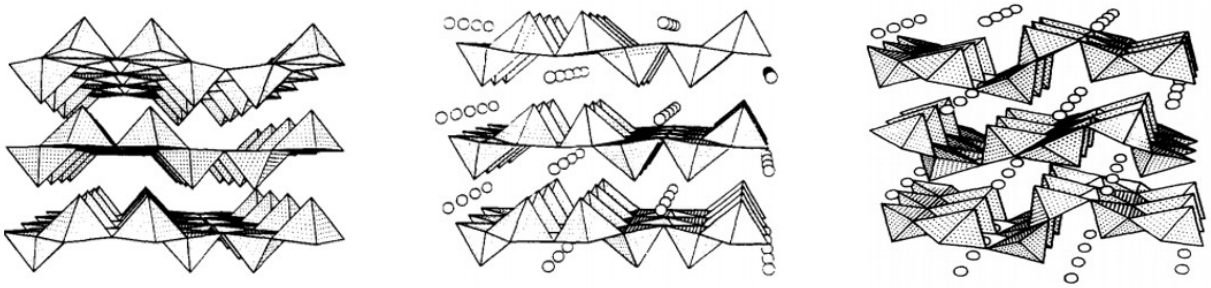

Figure 11. Crystal structure of different phases of $Li_xV_2O_5$ [56].

During the phase changes, the lattice parameters largely vary, particularly the “a” and “c” lattice parameter as can be seen in Table 2 . These changes in lattice parameter correspondingly produce significant changes in the elastic modulus, hardness, and stress accumulation during cycling, as described in detail in the following sections.

Table 2. $Li_xV_2O_5$ lattice parameters during lithiation [36]

Lattice Parameters	$Li_xV_2O_5$					
	x=0.0	x=0.4	x=1	x=1.4	x=2.0	x=3.0
a (Ă)	11.51	11.38	11.25	11.42	9.69	4.1
b (Ă)	3.56	3.57	3.6	3.57	3.6	4.1
c (Ă)	4.37	4.51	4.96	4.96	5.34	4.1

Nanoindentation

At the starred points labelled in Figure 10, electrodes were disconnected and tested by nanoindentation. Each phase was verified by XRD included in the Supplementary Information and

Table 3 shows the results of these experiments. Each sample exhibits a large standard deviation in its properties, which we attribute primarily to the surface morphology of the samples, as shown in Figure 12. This rough surface affects the accuracy of the area function used in nanoindentation and likely leads to an under representation of quantitative data; however, the qualitative trends of the data are still meaningful due to the large sample size. This large sample size also decreases the standard error of the mean and increases the probably that the reported average is an accurate representation of the sample mean. Each transition between phases, aside from the δ to γ transition, also passes the two sample Student T-Test with a p-value of <0.05 which shows that the properties of the phases are significantly different from one another.

Table 3. Mechanical Properties of $Li_xV_2O_5$

Phase	$Li_xV_2O_5$	Modulus	Modulus Std. Dev.	Modulus Std. Error of Mean	P value (from above test)	Hardness	Hardness Std. Dev.	Hardness Std. Error of Mean	P value (from above test)	n
		GPa								
α	0	17.8	7.5	0.82	----------	0.38	0.18	0.020	----------	84
ϵ	0.4	10.2	3.07	0.34	<0.0001	0.33	0.10	0.011	0.0389	80
δ	0.7	24.6	7.48	0.90	<0.0001	1.01	0.41	0.050	<0.0001	68
γ	2	22.1	10.96	0.99	0.0879	0.79	0.45	0.041	0.001	122
ω	3	34.7	14.67	1.56	<0.0001	0.42	0.42	0.045	<0.0001	88

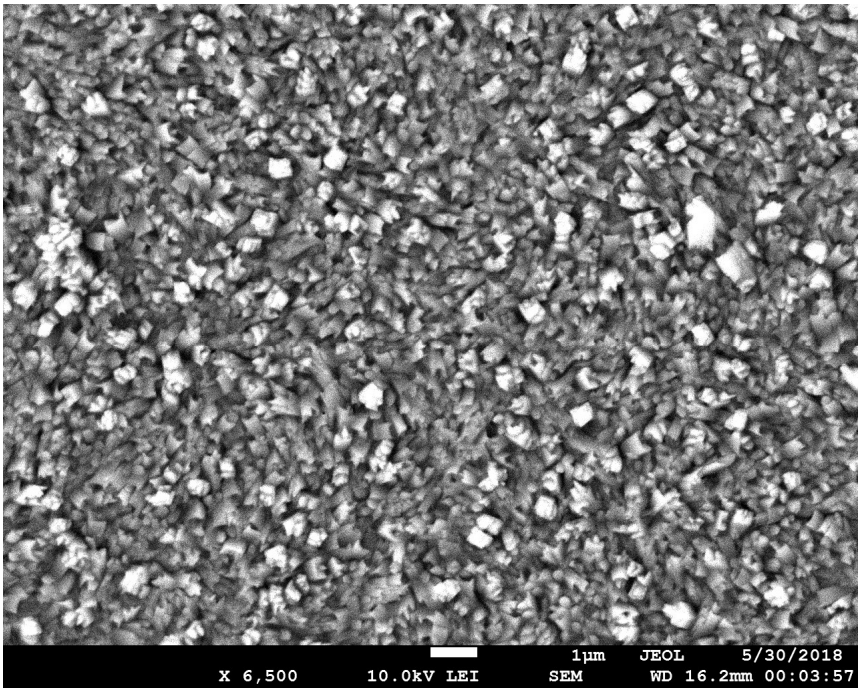

Figure 12. SEM image of rough surface morphology due to polycrystalline growth during sputtering

The results in

Table 3 are plotted in Figure 13 below to visualize the trends of modulus and hardness. As lithium concentration increases in the electrode, the modulus correspondingly shows a general increase. This trend likely occurs due to a combination of both increased interstitial Li ions and the evolution of crystal structure. The hardness of the electrode displays a general increase with lithium concentration through the δ phase followed by a decrease through the γ and ω phases. This trend may occur due to a mechanism similar to solid solution strengthening, in which initially inserted interstitial atoms harden a material, but eventually the behavior of the softer interstitial atoms begins to dominate the overall response in hardness.

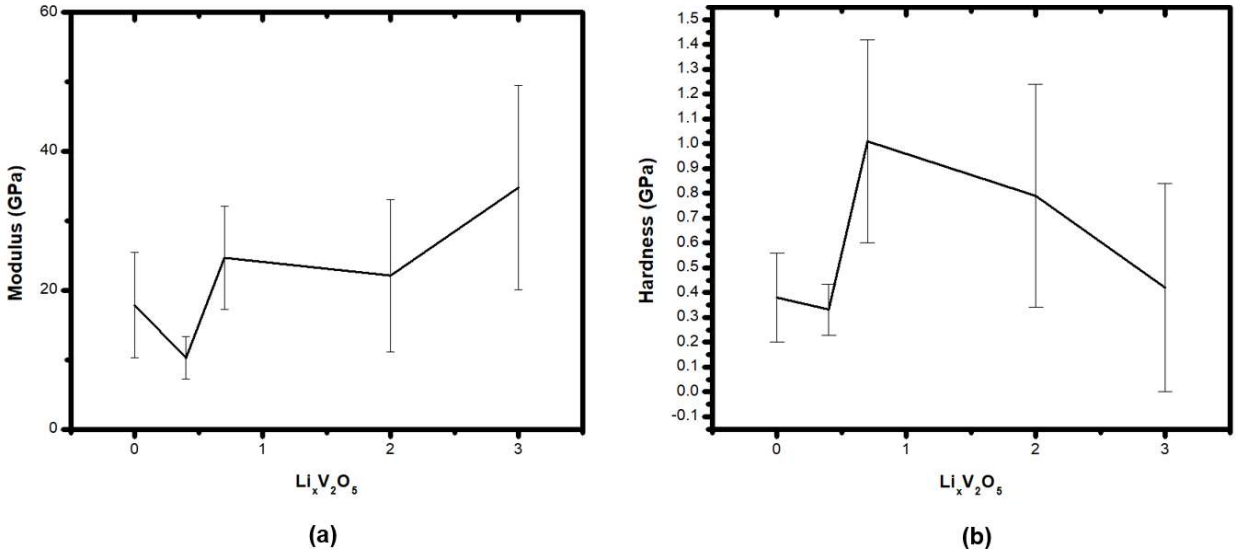

Figure 13. Modulus and Hardness vs. $Li_xV_2O_5$

Stress Analysis

After assembly of the quartz window split cell, the battery was rested for 14 hours to allow for equilibrium. The cell was then charged to 4V and was cycled twice through the $\alpha - \epsilon - \delta$ phases, the cycling of which is quite reversible. Finally, the cell was cycled twice all the way to the ω phase; in these cycles, irreversible structural changes occur after the first discharge.

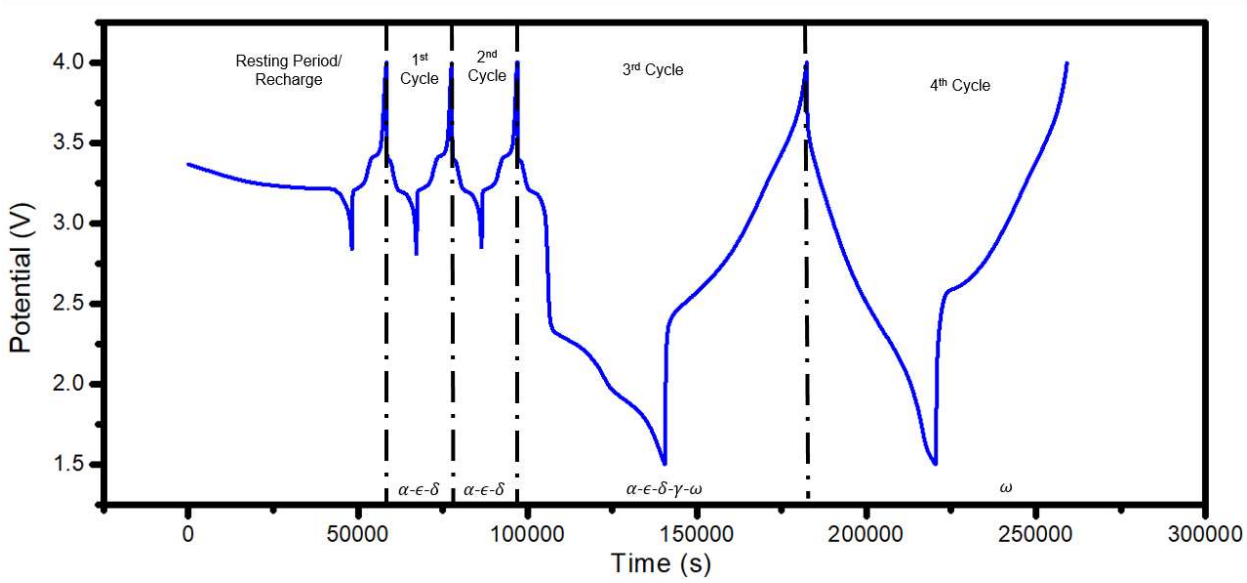

Figure 14. Electrochemical charge/discharge cycling curve of V_2O_5

As the electrode is cycled through the $\alpha - \epsilon - \delta$ phases the "a" lattice parameter, which is parallel to the surface of the film, monotonically decreases. While the "b" lattice parameter has the opposite trend and mitigates the effect, this decrease causes an overall trend of increasing tensile stress as can be seen in Figure 15. There are also a few inflection points, depicted in the red regions marked on the figure, where stress momentarily becomes more compressive before returning to a negative slope during discharge and the opposite during charging. These results agrees qualitatively with previously reported data in literature [33-36].

These inflection points seen in both of the $\alpha - \epsilon - \delta$ cycles and are correlated with sections of the charge/discharge curve where multiple phases coexist. This behavior possibly arises from some interphase solubility of Li ions when there are two co-present phases, causing an increase in compressive stress, but further insight is needed to conclusive find the cause of this phenomenon. Lithiating and delithiating through these phases also does not incur significant residual stresses

after each full cycle; this reversibility in stresses goes hand-in-hand with the electrochemical reversibility.

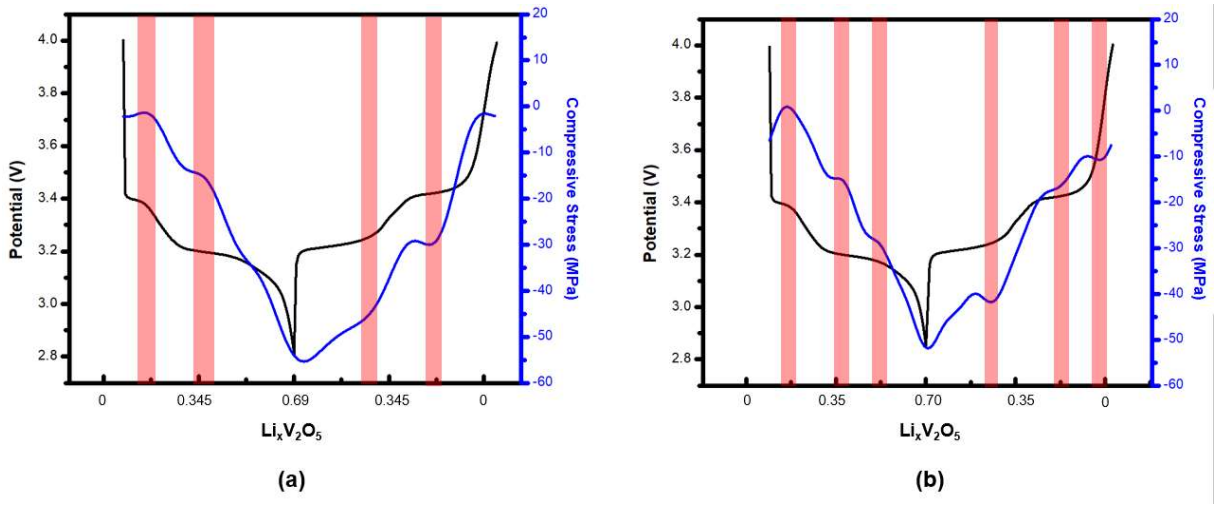

Figure 15. First (a) and second (b) cycles and associated stress accumulation

Figure 16 (a) depicts the first electrochemical cycle of the electrode through the full potential range (through the ω phase) and the corresponding stress accumulation. The same trend of overall tensile stress build up with sudden inflections occurs during the early part of the lithiation cycle, marked in red, with an additional inflection point in the range where δ transforms into γ. In the region starting at approximately x=1.47, designated in green, the stress correlates again with the "a" lattice parameter, which initially begins to lengthen, causing an increase in compressive stress, followed by a sharp contraction as it enters the ω phase. This large and irreversible structural change generates a large increase in the tensile stress in the film.

The overall trends observed in figure 16 (a) are in agreement with previously reported results of cycling through the ω phase, but differ in the magnitude of stress change. Both Scarminio

et al. and Jung et al. reported an increase of compressive stress in the range of x=1 to 2 that was greater than the tensile stress accumulated from x=0 to 1. In the case of Jung et al. this could be the result of cycling through the semi-reversible γ phase multiple times before cycling all the way to ω, but it is unclear what causes the discrepancy between the results of Scarminio et al. and those reported here [33, 36]

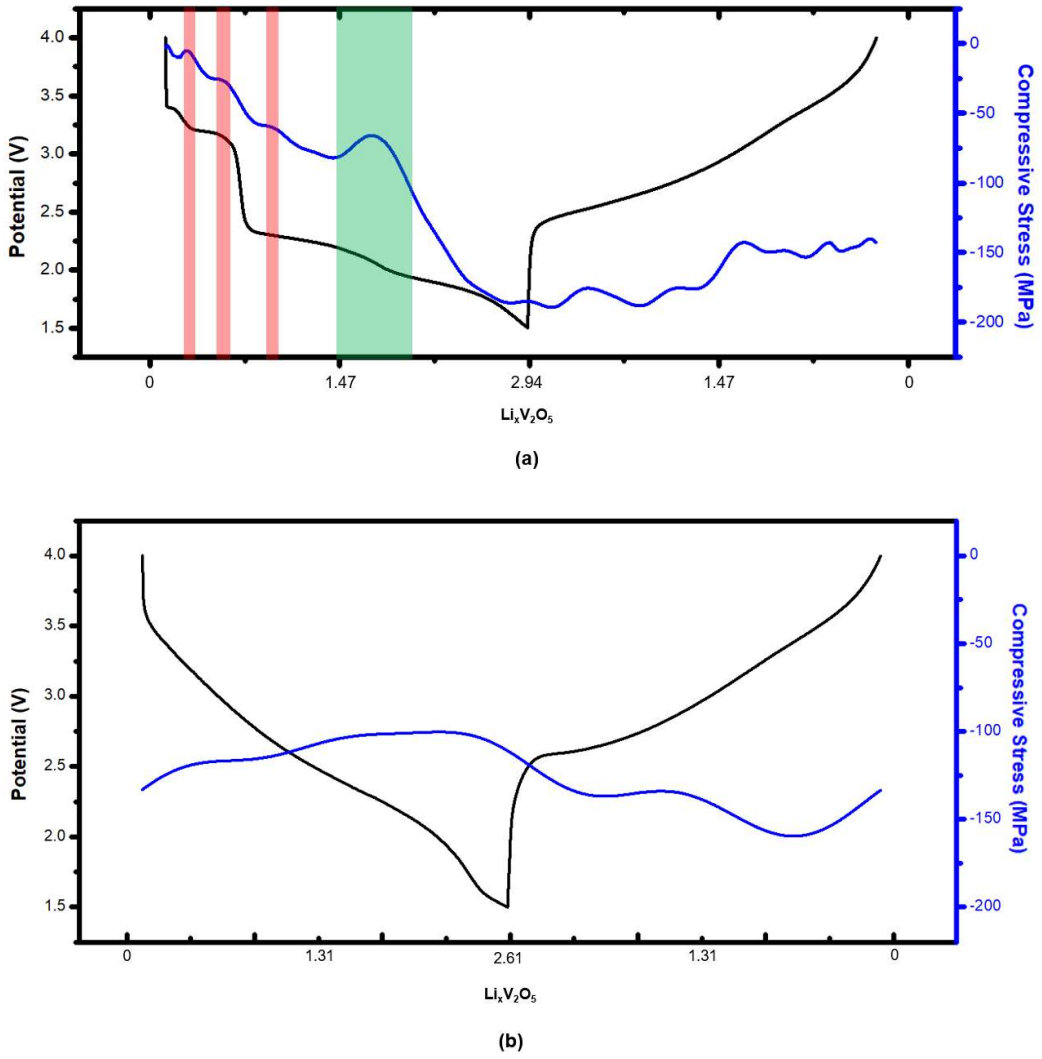

Figure 16. First (a) and second (b) cycle and over full discharge range (4-1.5 V) which results in an irreversible structural change after the first discharge.

During the charging section of Figure 16 (a) the electrode has transformed into a weakly crystalline "rock-salt" type structure. There is a complex stress accumulation that occurs during this charging period where there are many inflections of stress accumulation and a slight trend of more compressive stress. This could be due structural damage the occurred while transforming into the ω phase. More insight is needed about the kinetics of the material during lithiation to be able to definitively identify the cause of this behavior.

Figure 16 (b) shows the effect of permanent structural change of the V_2O_5 electrode on subsequent cycling. There is an 11.2% loss of capacity as well as significant residual stress that is not relaxed from the previous cycle. The ω phase, which no longer undergoes any phase transformations during lithiation, becomes more compressive as more lithium is added which is the opposite of previous cycles and agrees with trends previously reported [33, 36]. The overall stress accumulation in this cycle is very comparable to that seen in amorphous materials such as silicon and implies a similar structure [57].

Future Work

Most of the quantitative analysis provided above assumes a thin, homogeneous, and smooth film. Figure 12 shows that the morphology of the film tested was a rough polycrystalline film that is far from ideal for treatment as a thin film. For nanoindentation, this surface roughness greatly impacts the calculated area function that is used in determining elasticity and hardness measurements. The morphology of the film also appears to be made up of discrete or loosely connected pillars, which likely affect the stress calculation used in the MOS measurements. If these are indeed pillars, they would only be constrained at their base, with room to expand laterally further away from the base. This situation would cause an underestimation of the stress developed

in a real thin film, as only a fraction of the force produced from lithiation would be transferred to the substrate here (as can be seen from the work in Chapter 2.)

The future work for increasing the confidence in and accuracy of the reported results centers around improving the morphology to more closely resemble a thin film. We believe that such a morphology can be achieved by changing sputtering parameters such as process pressure and temperature, cooling rates, or first creating an amorphous film and then annealing it to create the desired crystal structure.

CHAPTER IV

CONCLUDING REMARKS*

Using finite element simulations in ABAQUS, we have investigated fractures at the interface between a NW electrode and a CC in LIBs as a function of geometric and material parameters. We have found that the energy release rate decays to zero as the crack length approaches the radius of the NW. As a result, the crack either (1) does not propagate at all or (2) arrests at a length smaller than the radius of the NW. However, crack initiation has detrimental effects on the system in that it can (1) increase the electrical resistance of the system and/or (2) increase the susceptibility of the NW to complete delamination upon subsequent external mechanical loading.

We also find that the energy release rate is independent of the aspect ratio but increases linearly with the radius of the NW. Furthermore, we find that plasticity in the NW during lithiation significantly affects the energy release rate; materials with relatively low yield strengths limit the stresses build up in the system, thus reducing crack-driving forces. As a final note, our analysis of crack initiation depends on the value of the interfacial energy of the NW/CC interface. Because relatively few interfacial energies have been determined in these systems, we hope this study will motivate future experimental and first-principles simulations to determine the interfacial energies of materials of practical relevance in LIB systems.

*Part of this chapter has been reprinted with permission from "Interfacial Fracture of Nanowire Electrodes of Lithium-Ion Batteries" by G. R. Hardin, Y. Zhang, C. D. Fincher et al, 2017. JOM Journal of the Minerals, Metals and Materials Society, 69, 9, Copyright 2017 by Springer Nature

Utilizing nanoindentation and MOS measurements, we calculated the modulus, hardness, and stress evolution of $Li_xV_2O_5$ during electrochemical cycling through the entire lithiation range. We found that the modulus shows a general and gradual increase with further lithiation, while hardness sees a general increase through the δ phase followed by a monotonic decrease. The stress of the film correlates well with the change in the "a" lattice parameter, but includes some interesting sudden inflections when multiple phases coexist. After transforming into the weakly crystalline rock-salt ω phase, the films sees an increase in compressive stress with lithium insertion. During charging, this phase displays amorphous like behavior likely due to the structural damage incurred during the irreversible phase transformation.

Future work in this area should target changing the morphology of the produced V_2O_5 film to make it more closely resemble a homogenous thin film. Doing so would improve the accuracy of the assumptions made when calculating modulus, hardness, and stress and would increase the accuracy of the reported data.

REFERENCES

1. Armand, M.; Tarascon, J. M., Building better batteries. *Nature* **2008,** *451*, 652.

2. Service, R. F., Outlook Brightens for Plastic Solar Cells. *Science* **2011,** *332* (6027), 293-293.

3. Pharr, M.; Suo, Z.; Vlassak, J. J., Measurements of the Fracture Energy of Lithiated Silicon Electrodes of Li-Ion Batteries. *Nano Letters* **2013,** *13* (11), 5570-5577.

4. Ellis, B. L.; Lee, K. T.; Nazar, L. F., Positive Electrode Materials for Li-Ion and Li-Batteries. *Chemistry of Materials* **2010,** *22* (3), 691-714.

5. Marom, R.; Amalraj, S. F.; Leifer, N.; Jacob, D.; Aurbach, D., A review of advanced and practical lithium battery materials. *Journal of Materials Chemistry* **2011,** *21* (27), 9938-9954.

6. Takamura, T.; Ohara, S.; Uehara, M.; Suzuki, J.; Sekine, K., A vacuum deposited Si film having a Li extraction capacity over 2000 mAh/g with a long cycle life. *J. Power Sources* **2004,** *129* (1), 96-100.

7. Chan, C. K.; Peng, H.; Liu, G.; McIlwrath, K.; Zhang, X. F.; Huggins, R. A.; Cui, Y., High-performance lithium battery anodes using silicon nanowires. *Nat. Nanotechnol.* **2008,** *3* (1), 31-35.

8. Wu, H.; Zheng, G.; Liu, N.; Carney, T. J.; Yang, Y.; Cui, Y., Engineering Empty Space between Si Nanoparticles for Lithium-Ion Battery Anodes. *Nano Lett.* **2012,** *12* (2), 904-909.

9. Teki, R.; Datta, M. K.; Krishnan, R.; Parker, T. C.; Lu, T.-M.; Kumta, P. N.; Koratkar, N., Nanostructured Silicon Anodes for Lithium Ion Rechargeable Batteries. *Small* **2009,** *5* (20), 2236-2242.

10. Nguyen, H. T.; Yao, F.; Zamfir, M. R.; Biswas, C.; So, K. P.; Lee, Y. H.; Kim, S. M.; Cha, S. N.; Kim, J. M.; Pribat, D., Highly Interconnected Si Nanowires for Improved Stability Li-Ion Battery Anodes. *Adv. Energy Mater.* **2011,** *1* (6), 1154-1161.

11. Laïk, B.; Eude, L.; Pereira-Ramos, J.-P.; Cojocaru, C. S.; Pribat, D.; Rouvière, E., Silicon nanowires as negative electrode for lithium-ion microbatteries. *Electrochim. Acta* **2008,** *53* (17), 5528-5532.

12. Zhao, K.; Pharr, M.; Vlassak, J. J.; Suo, Z., Inelastic hosts as electrodes for high-capacity lithium-ion batteries. *J. Appl. Phys.* **2011,** *109*, 016110.

13. Armstrong, A. R.; Armstrong, G.; Canales, J.; García, R.; Bruce, P. G., Lithium-Ion Intercalation into TiO2-B Nanowires. *Adv. Mater.* **2005,** *17* (7), 862-865.

14. Park, M. S.; Wang, G. X.; Kang, Y. M.; Wexler, D.; Dou, S. X.; Liu, H. K., Preparation and Electrochemical Properties of SnO2 Nanowires for Application in Lithium-Ion Batteries. *Angew. Chem.* **2007,** *119* (5), 764-767.

15. Li, Y.; Tan, B.; Wu, Y., Mesoporous Co3O4 Nanowire Arrays for Lithium Ion Batteries with High Capacity and Rate Capability. *Nano Lett.* **2008,** *8* (1), 265-270.

16. Huang, J. Y.; Zhong, L.; Wang, C. M.; Sullivan, J. P.; Xu, W.; Zhang, L. Q.; Mao, S. X.; Hudak, N. S.; Liu, X. H.; Subramanian, A.; Fan, H.; Qi, L.; Kushima, A.; Li, J., In Situ Observation of the Electrochemical Lithiation of a Single SnO_2 Nanowire Electrode. *Science* **2010,** *330* (6010), 1515-1520.

17. Kennedy, T.; Mullane, E.; Geaney, H.; Osiak, M.; O'Dwyer, C.; Ryan, K. M., High-Performance Germanium Nanowire-Based Lithium-Ion Battery Anodes Extending over 1000

Cycles Through in Situ Formation of a Continuous Porous Network. *Nano Lett.* **2014,** *14* (2), 716-723.

18. Ryu, I.; Choi, J. W.; Cui, Y.; Nix, W. D., Size-dependent fracture of Si nanowire battery anodes. *J. Mech. Phys. Solids.* **2011,** *59* (9), 1717-1730.

19. Liu, X. H.; Zheng, H.; Zhong, L.; Huang, S.; Karki, K.; Zhang, L. Q.; Liu, Y.; Kushima, A.; Liang, W. T.; Wang, J. W.; Cho, J.-H.; Epstein, E.; Dayeh, S. A.; Picraux, S. T.; Zhu, T.; Li, J.; Sullivan, J. P.; Cumings, J.; Wang, C.; Mao, S. X.; Ye, Z. Z.; Zhang, S.; Huang, J. Y., Anisotropic Swelling and Fracture of Silicon Nanowires during Lithiation. *Nano Lett.* **2011,** *11* (8), 3312-3318.

20. Granqvist, C. G., Electrochromics for smart windows: Oxide-based thin films and devices. *Thin Solid Films* **2014,** *564*, 1-38.

21. Wu, C.; Xie, Y., Promising vanadium oxide and hydroxide nanostructures: from energy storage to energy saving. *Energy & Environmental Science* **2010,** *3* (9), 1191-1206.

22. Wu, C.; Feng, F.; Xie, Y., Design of vanadium oxide structures with controllable electrical properties for energy applications. *Chemical Society Reviews* **2013,** *42* (12), 5157-5183.

23. Liu, J.; Wang, X.; Peng, Q.; Li, Y., Preparation and gas sensing properties of vanadium oxide nanobelts coated with semiconductor oxides. *Sensors and Actuators B: Chemical* **2006,** *115* (1), 481-487.

24. Jerominek, H.; Picard, F.; Vincent, D. In *Vanadium oxide films for optical switching and detection*, SPIE: 1993; p 8.

25. Mai, L.; Xu, L.; Han, C.; Xu, X.; Luo, Y.; Zhao, S.; Zhao, Y., Electrospun Ultralong Hierarchical Vanadium Oxide Nanowires with High Performance for Lithium Ion Batteries. *Nano Letters* **2010,** *10* (11), 4750-4755.

26. Sakamoto, J. S.; Dunn, B., Vanadium oxide-carbon nanotube composite electrodes for use in secondary lithium batteries. *Journal of the Electrochemical Society* **2002,** *149* (1), A26-A30.

27. Wu, Y.; Zhu, P.; Zhao, X.; Reddy, M.; Peng, S.; Chowdari, B.; Ramakrishna, S., Highly improved rechargeable stability for lithium/silver vanadium oxide battery induced via electrospinning technique. *Journal of Materials Chemistry A* **2013,** *1* (3), 852-859.

28. West, K.; Zachau-Christiansen, B.; Østergård, M. J. L.; Jacobsen, T., Vanadium oxides as electrode materials for rechargeable lithium cells. *Journal of Power Sources* **1987,** *20* (1), 165-172.

29. Chou, S.-L.; Wang, J.-Z.; Sun, J.-Z.; Wexler, D.; Forsyth, M.; Liu, H.-K.; MacFarlane, D. R.; Dou, S.-X., High Capacity, Safety, and Enhanced Cyclability of Lithium Metal Battery Using a V2O5 Nanomaterial Cathode and Room Temperature Ionic Liquid Electrolyte. *Chemistry of Materials* **2008,** *20* (22), 7044-7051.

30. Vivier, V.; Farcy, J.; Pereira-Ramos, J.-P., Electrochemical lithium insertion in sol-gel crystalline vanadium pentoxide thin films. *Electrochimica Acta* **1998,** *44* (5), 831-839.

31. Geryl, K. N. I. V.; Detavernier, C. p., Atomic layer deposition of vanadium oxides for lithium-ion batteries. 2014.: 2014.

32. Mattelaer, F.; Geryl, K.; Rampelberg, G.; Dobbelaere, T.; Dendooven, J.; Detavernier, C., Atomic layer deposition of vanadium oxides for thin-film lithium-ion battery applications. *RSC Advances* **2016,** *6* (115), 114658-114665.

33. Scarminio, J.; Talledo, A.; Andersson, A. A.; Passerini, S.; Decker, F., Stress and electrochromism induced by Li insertion in crystalline and amorphous V2O5 thin film electrodes. *Electrochimica Acta* **1993,** *38* (12), 1637-1642.

34. Talledo, A.; Granqvist, C. G., Electrochromic vanadium–pentoxide–based films: Structural, electrochemical, and optical properties. *Journal of Applied Physics* **1995,** *77* (9), 4655-4666.

35. Jung, H.; Gerasopoulos, K.; Talin, A. A.; Ghodssi, R., In situ characterization of charge rate dependent stress and structure changes in V2O5 cathode prepared by atomic layer deposition. *Journal of Power Sources* **2017,** *340*, 89-97.

36. Jung, H.; Gerasopoulos, K.; Talin, A. A.; Ghodssi, R., A platform for in situ Raman and stress characterizations of V2O5 cathode using MEMS device. *Electrochimica Acta* **2017,** *242*, 227-239.

37. Huang, S.; Zhu, T., Atomistic mechanisms of lithium insertion in amorphous silicon. *J. Power Sources* **2011,** *196* (7), 3664-3668.

38. Jerliu, B.; Hüger, E.; Dörrer, L.; Seidlhofer, B. K.; Steitz, R.; Oberst, V.; Geckle, U.; Bruns, M.; Schmidt, H., Volume Expansion during Lithiation of Amorphous Silicon Thin Film Electrodes Studied by In-Operando Neutron Reflectometry. *J. Phys. Chem. C* **2014,** *118* (18), 9395-9399.

39. Pharr, M.; Zhao, K.; Wang, X.; Suo, Z.; Vlassak, J. J., Kinetics of Initial Lithiation of Crystalline Silicon Electrodes of Lithium-Ion Batteries. *Nano Letters* **2012,** *12* (9), 5039-5047.

40. McDowell, M. T.; Lee, S. W.; Harris, J. T.; Korgel, B. A.; Wang, C.; Nix, W. D.; Cui, Y., In Situ TEM of Two-Phase Lithiation of Amorphous Silicon Nanospheres. *Nano Letters* **2013,** *13* (2), 758-764.

41. Wang, J. W.; He, Y.; Fan, F.; Liu, X. H.; Xia, S.; Liu, Y.; Harris, C. T.; Li, H.; Huang, J. Y.; Mao, S. X.; Zhu, T., Two-Phase Electrochemical Lithiation in Amorphous Silicon. *Nano Letters* **2013,** *13* (2), 709-715.

42. Chen, L.; Fan, F.; Hong, L.; Chen, J.; Ji, Y.; Zhang, S.; Zhu, T.; Chen, L., A phase-field model coupled with large elasto-plastic deformation: application to lithiated silicon electrodes. *Journal of The Electrochemical Society* **2014,** *161* (11), F3164-F3172.

43. Hardin, G. R.; Zhang, Y.; Fincher, C. D.; Pharr, M., Interfacial Fracture of Nanowire Electrodes of Lithium-Ion Batteries. *JOM* **2017,** *69* (9), 1519-1523.

44. Choi, Y. S.; Pharr, M.; Oh, K. H.; Vlassak, J. J., A simple technique for measuring the fracture energy of lithiated thin-film silicon electrodes at various lithium concentrations. *Journal of Power Sources* **2015,** *294*, 159-166.

45. Zhao, K.; Pharr, M.; Vlassak, J. J.; Suo, Z., Fracture of electrodes in lithium-ion batteries caused by fast charging. *Journal of Applied Physics* **2010,** *108* (7), 073517.

46. Stournara, M. E.; Xiao, X.; Qi, Y.; Johari, P.; Lu, P.; Sheldon, B. W.; Gao, H.; Shenoy, V. B., Li Segregation Induces Structure and Strength Changes at the Amorphous Si/Cu Interface. *Nano Lett.* **2013,** *13* (10), 4759-4768.

47. Thiagarajan, S.; Thaiyan, M.; Ganesan, R., Physical vapor deposited highly oriented V 2 O 5 thin films for electrocatalytic oxidation of hydrazine. *RSC Advances* **2016,** *6* (86), 82581-82590.

48. Shimizu, Y.; Nagase, K.; Miura, N.; Yamazoe, N., New preparation process of V2O5 thin film based on spin-coating from organic vanadium solution. *Japanese Journal of applied physics* **1990,** *29* (9A), L1708.

49. Benmoussa, M.; Ibnouelghazi, E.; Bennouna, A.; Ameziane, E., Structural, electrical and optical properties of sputtered vanadium pentoxide thin films. *Thin solid films* **1995,** *265* (1-2), 22-28.

50. Horrocks, G. A.; Likely, M. F.; Velazquez, J. M.; Banerjee, S., Finite size effects on the structural progression induced by lithiation of V 2 O 5: a combined diffraction and Raman spectroscopy study. *Journal of Materials Chemistry A* **2013,** *1* (48), 15265-15277.

51. Baddour-Hadjean, R.; Pereira-Ramos, J.-P., Raman microspectrometry applied to the study of electrode materials for lithium batteries. *Chemical reviews* **2009,** *110* (3), 1278-1319.

52. Hay, J.; Crawford, B., Measuring substrate-independent modulus of thin films. *Journal of Materials Research* **2011,** *26* (6), 727-738.

53. Oliver, W. C.; Pharr, G. M., An improved technique for determining hardness and elastic modulus using load and displacement sensing indentation experiments. *Journal of materials research* **1992,** *7* (6), 1564-1583.

54. Stoney, G., The tension of metallic films deposited by electrolysis. *Proceedings of the Royal Society of London. Series A* **1909,** *82* (553), 172-175.

55. Nix, W. D., Mechanical properties of thin films. *Metallurgical Transactions A* **1989,** *20* (11), 2217.

56. Delmas, C.; Cognac-Auradou, H.; Cocciantelli, J. M.; Ménétrier, M.; Doumerc, J. P., The LixV2O5 system: An overview of the structure modifications induced by the lithium intercalation. *Solid State Ionics* **1994,** *69* (3), 257-264.

57. Zhao, K.; Tritsaris, G. A.; Pharr, M.; Wang, W. L.; Okeke, O.; Suo, Z.; Vlassak, J. J.; Kaxiras, E., Reactive Flow in Silicon Electrodes Assisted by the Insertion of Lithium. *Nano Letters* **2012,** *12* (8), 4397-4403.

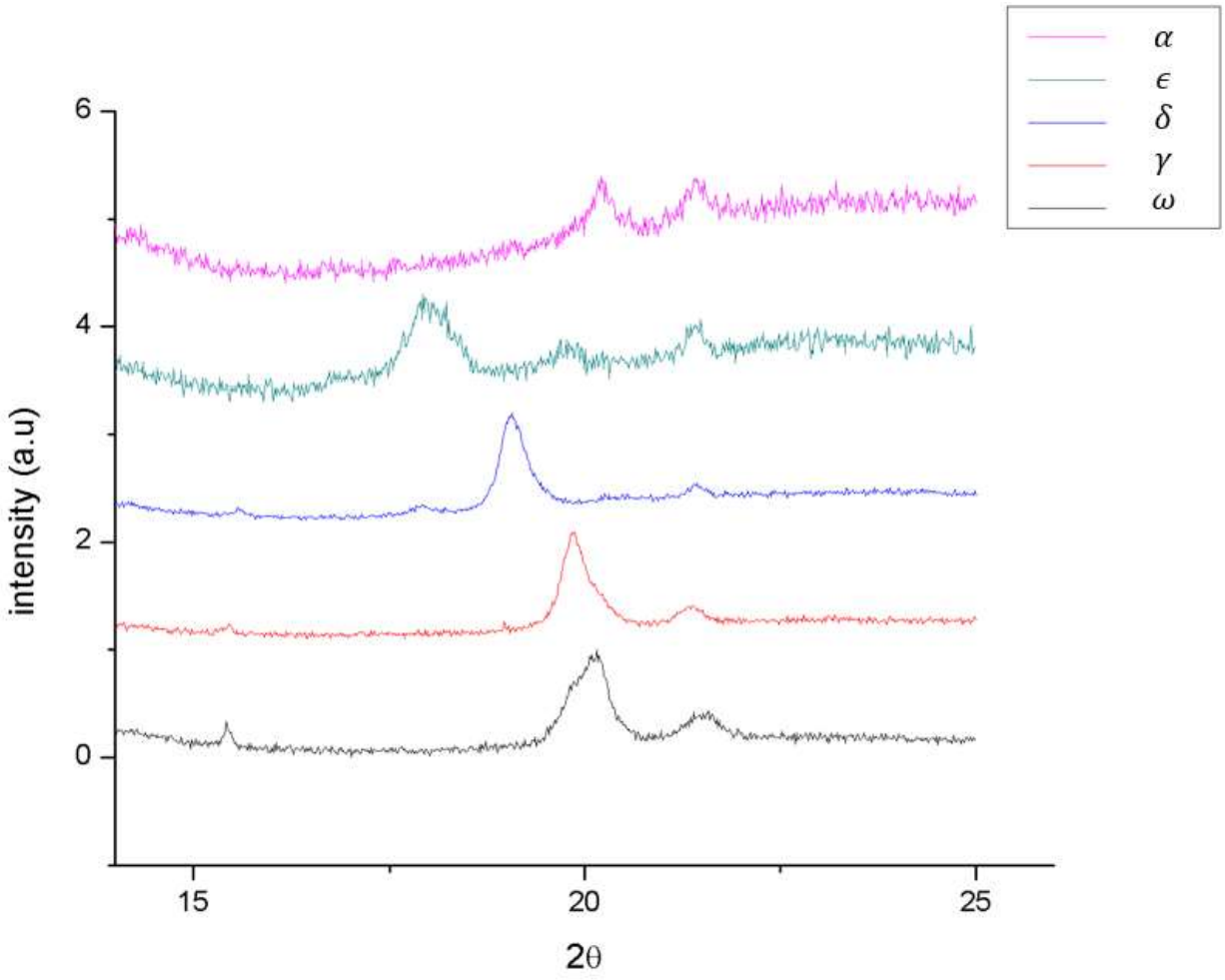

Figure 17. Raw XRD of $Li_xV_2O_5$ phases that underwent nanoindentation testing